energies

MDPI

Article

Quadrature Voltage Compensation in the Isolated Multi-Modular Converter

Cristian Verdugo [1,*], Jose Ignacio Candela [1] and Pedro Rodriguez [1,2]

[1] Electrical Department, Technical University of Catalonia, 08222 Terrassa, Spain; candela@ee.upc.edu (J.I.C.); pedro.rodriguez@upc.edu (P.R.)

[2] Luxembourg Institute of Science and Technology (LIST) , 4362 Belval, Luxembourg; pedro.rodriguez@list.lu

* Correspondence: cristian.andres.verdugo@upc.edu

Abstract: Series connections of modules in cascaded multilevel converters are prone to power imbalances due to voltage differences on their DC side. When modules are connected to direct current (DC) sources, such as photovoltaic panels, the capability of withstanding power imbalances is crucial for generating the maximum power. In order to provide a possible solution for this requirement, this paper proposes a control strategy called Quadrature Voltage Compensation, which allows a wide range of power imbalances. The proposed control strategy regulates the power by introducing a circulating current between the arms and a phase angle in the output voltage. The impact of the circulating current and its effect on the phase voltage are studied. To highlight the features of the proposed strategy, an analytical model based on vector superposition is also described, demonstrating the strong capability of tolerating power differences. Finally, to validate the effectiveness of the Quadrature Voltage Compensation, simulation and experimental results are presented for a three-phase isolated multi-modular converter.

Keywords: cascaded-transformer multilevel inverter; energy balance operation; isolated multi-modular converter

check for updates

Citation: Verdugo, C.; Candela, J.I.; Rodriguez, P. Quadrature Voltage Compensation in an Isolated Multi-Modular Converter. *Energies* **2021**, *14*, 529. https://doi.org/10.3390/en14030529

Academic Editor: André Madureira

Received: 1 November 2020

Accepted: 12 January 2021

Published: 20 January 2021

1. Introduction

Power generation based on renewable energies has increased over the last years [1]. That is also the case of photovoltaic (PV) power plants, which demand efficient and reliable conversion systems to operate at maximum power levels. In this regard, multicell converters have become the most attractive solutions for providing modularity, wide power operation, and a large voltage range [2–4]. Of the various multicell topologies, cascaded multilevel converters are the most suitable configurations for large PV power plants [5–9], since they can connect individual power modules to groups of PV panels. However, when several modules are connected in series, galvanic isolation is required to fulfill insulation constraints.

Cascaded-transformer multilevel inverters (CTMIs) provide isolation through low-frequency transformers [10–15]. They have several H-bridge converters connected in parallel to a single direct current (DC) source, while the cascaded connection is made on the secondary side of the transformers. Although CTMIs require bulky transformers, they are robust and highly reliable, an important aspect to consider in PV applications. Different analyses based on CTMIs for PV applications have been presented in the past. In [14,15], an asymmetric configuration with different turn ratios was proposed in order to increase the number of stepped voltage levels; the harmonic content was reduced while the voltage quality was improved. In [10], a modified CTMI based on a three-phase configuration was proposed for PV applications. The configuration had three parallel branches to define the three phases formed by several modules connected in series, all of them linked to the same DC source. More analyses based on CTMIs are presented in [16,17]. However, the single DC source in classical CTMI configurations limits their application in PV power plants where several PV strings are used to generate large power levels. In order to distribute the power provided by several PV panels, a different approach was proposed in [18]. This configuration is called an isolated multi-modular converter (IMMC), and it is formed by two arms in parallel with several modules connected to independent PV strings, thus making higher voltage and power levels possible.

As non-uniform irradiance and temperature changes may affect the power that is generated, power converters based on cascaded configurations have to cope with possible imbalance operations. In order to operate under such scenarios, several control strategies have previously been proposed for cascaded converters. In [19], a control strategy based on a zero-sequence injection was presented. This control strategy compensates power imbalances between phases by introducing a zero-sequence component. In [20], the proposed strategy distributes the power between modules by introducing the cosine value of the current phase angle in the denominator of the power compensation. This operation makes the control very sensitive to disturbances due to the zero-crossing point in the cosine value. Another control strategy proposed for cascaded multilevel converters was presented in [21]. The controller regulates the modulated voltage based on a voltage vector superposition, in which the phase current is used to regulate the absorbed active power. To operate under power imbalances in an IMMC, a control strategy was presented in [18]. This strategy modifies the modulated voltage amplitude according to the energy level of each module. Hence, modules with higher power increase their modulated voltage amplitudes, while modules with lower power decrease their voltage amplitudes. However, this strategy is limited when modules operate close to overmodulation, thus reducing the operating range of the converter.

The capability of tolerating large power imbalances in PV applications based on cascaded converters is an important point to consider. Therefore, a control strategy that is able to provide a wide range of power imbalances is necessary. This paper proposes a control strategy for an IMMC called Quadrature Voltage Compensation (QVC). The control strategy regulates the power of each module based on a circulating current flowing through the arms and a phase angle introduced in the output voltage. Due to the series connection of the modules, the quadrature component of the circulating current is used to regulate the power imbalance in all modules at the same time, while the phase angle compensation is embedded inside every module to regulate the power in each of them.

The rest of the paper is organized as follows. Section 2 describes the main principle of the IMMC in matrix form notation. Then, an instantaneous power analysis is introduced to demonstrate the effect of the output and circulating currents in the power flow. Section 3 presents the basis of the proposed QVC, including a power analysis under different phase angles and circulating current levels. Section 4 demonstrates the effectiveness of the proposed control with simulation and experimental results and compares the QVC with the amplitude voltage compensation (AVC) introduced in [18]. Finally, Section 5 summarizes the work.

2. IMMC Model

The three-phase IMMC is a multilevel converter with alternating current (AC) transformers and two arms connected in parallel, as seen in Figure 1. The current arms can be decomposed into two components: the output current injected into the grid and the circulating current flowing through the arms. The latter current component arrives as a consequence of power imbalances without introducing any effect on the output power [18]. The series connections of the modules are electrically connected through the secondary side of low-frequency transformers, thus providing galvanic isolation and eliminating leakage current components. Using this configuration, the DC sources connected to each module are isolated.

Based on the current and voltage descriptions given in Figure 1, signals $i_{u,abc}$ and $i_{l,abc}$ represent the three-phase currents in the upper and lower arms, while $i_{o,abc}$ and $i_{c,abc}$ are the three-phase output and circulating currents, respectively. The voltage v_o is the output voltage given by the series connection of the modules, while $v_{dci,j}$ represents the voltage measured on the DC side of module j in arm i. The dynamic model per phase of the IMMC was previously studied in [18]. However, using the matrix form notation introduced in Section 2.1, the IMMC model can be simplified.

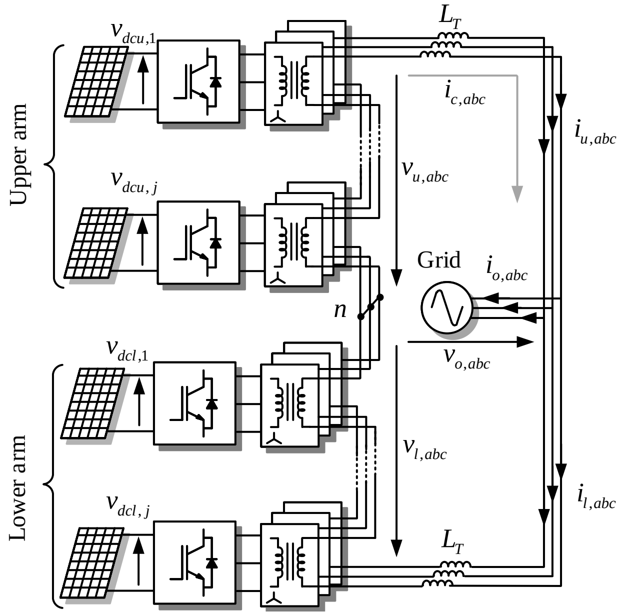

Figure 1. Three-phase isolated multi-modular converter (IMMC).

2.1. Matrix Form Notation

In order to determine the relationship between the current and DC voltages, the IMMC is simplified using the electrical circuit illustrated in Figure 2. Because the three phases have similar characteristics, only one phase is illustrated for modeling purposes. Each module is replaced by a controlled voltage source $v_{i,k,j}$, where k is the phase $\{a, b, c\}$ and j is the number of the module. The inductance L_T represents the total inductance given by the series connection of low-frequency transformers and R_T represents the losses of the arm. The grid voltage is simplified by an AC voltage source connected in series to an equivalent resistor R_s and inductance L_s.

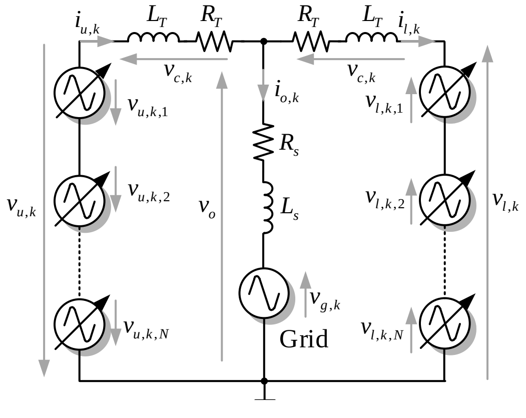

Figure 2. Equivalent electrical circuit per phase.

Using the equivalent model, six equations can be derived to represent the complete behavior of the converter. According to the current and voltage definition given by Figure 2, the dynamic model per phase of the upper and lower arms yields:

$$v_{u,k} = -L_T \frac{d}{dt} i_{u,k} - R_T i_{u,k} - v_{o,k} \tag{1a}$$

$$v_{l,k} = -L_T \frac{d}{dt} i_{l,k} - R_T i_{l,k} + v_{o,k}. \tag{1b}$$

Voltages $v_{u,k}$ and $v_{l,k}$ are the total voltage arms, while $v_{o,k}$ is the voltage in the converter terminals. By combining the previous expressions, the dynamic model can be rewritten in matrix notation as follows.

$$\begin{bmatrix} \mathbf{v_u} \\ \mathbf{v_l} \end{bmatrix} = -\begin{bmatrix} \mathbf{L_T} & 0 \\ 0 & \mathbf{L_T} \end{bmatrix} \frac{d}{dt} \begin{bmatrix} \mathbf{i_u} \\ \mathbf{i_l} \end{bmatrix} - \begin{bmatrix} \mathbf{R_T} & 0 \\ 0 & \mathbf{R_T} \end{bmatrix} \begin{bmatrix} \mathbf{i_u} \\ \mathbf{i_l} \end{bmatrix} + \begin{bmatrix} -\mathbf{v_o} \\ \mathbf{v_o} \end{bmatrix}, \tag{2}$$

where $\mathrm{R_T}$ and $\mathrm{L_T}$ are 3×3 diagonal matrices. On the other hand, the sinusoidal current and voltage components are represented as vectors by:

$$\mathbf{i_x} = \begin{bmatrix} i_{x,a} \\ i_{x,b} \\ i_{x,c} \end{bmatrix} \qquad \mathbf{v_x} = \begin{bmatrix} v_{x,a} \\ v_{x,b} \\ v_{x,c} \end{bmatrix}, \tag{3}$$

where x denotes either an arm or output component.

The symmetry provided in Equation (2) for the upper and lower arms can be used to obtain two decoupled models based on the output and circulating current definitions. The relationship between the current arms and the output and circulating current are given by:

$$\begin{bmatrix} \mathbf{i}_{\mathbf{o},\alpha\beta 0} \\ \mathbf{i}_{\mathbf{c},\alpha\beta 0} \end{bmatrix} = \mathbf{T_M} \begin{bmatrix} \mathbf{i_u} \\ \mathbf{i_u} \end{bmatrix} \qquad \begin{bmatrix} \mathbf{i_u} \\ \mathbf{i_l} \end{bmatrix} = \mathbf{T_M^{-1}} \begin{bmatrix} \mathbf{i}_{\mathbf{o},\alpha\beta 0} \\ \mathbf{i}_{\mathbf{c},\alpha\beta 0} \end{bmatrix}. \tag{4}$$

The decoupled matrix $\mathrm{T_M}$ is used to transform the current arms in $\alpha\beta 0$ components. This matrix is defined based on the Clark transform $\mathrm{T_c}$.

$$\mathbf{T_M} = \begin{bmatrix} \mathrm{T_c} & -\mathrm{T_c} \\ \mathrm{T_c}/2 & \mathrm{T_c}/2 \end{bmatrix} \tag{5}$$

By applying the inverse matrix transformation $\mathrm{T_M^{-1}}$ to the dynamic model presented in Equation (2), the output and circulating currents can be rewritten as:

$$\begin{bmatrix} \mathbf{v_u} \\ \mathbf{v_l} \end{bmatrix} = -\begin{bmatrix} \mathbf{L_T} & 0 \\ 0 & \mathbf{L_T} \end{bmatrix} \frac{d}{dt} \mathbf{T_M^{-1}} \begin{bmatrix} \mathbf{i}_{\mathbf{o},\alpha\beta} \\ \mathbf{i}_{\mathbf{c},\alpha\beta} \end{bmatrix} - \begin{bmatrix} \mathbf{R_T} & 0 \\ 0 & \mathbf{R_T} \end{bmatrix} \mathbf{T_M^{-1}} \begin{bmatrix} \mathbf{i}_{\mathbf{o},\alpha\beta} \\ \mathbf{i}_{\mathbf{c},\alpha\beta} \end{bmatrix} - \mathbf{T_M^{-1}} \begin{bmatrix} \mathbf{2v}_{\mathbf{o},\alpha\beta} \\ 0 \end{bmatrix}. \tag{6}$$

The matrix transformation is used to rotate the output voltage in abc to the $\alpha\beta$ reference frame. It is important to mention that the 0 component of the output current is zero, as the common point n of the converter is not connected to the grid.

By defining the voltage difference between $\mathrm{v_u}$ and $\mathrm{v_l}$ as equal to $2\mathrm{v_s}$ and the addition of $\mathrm{v_u}/2$ and $\mathrm{v_l}/2$ as equal to $\mathrm{v_c}$, the relationship between the matrix transformation and the voltage arms is reduced to:

$$\begin{bmatrix} \mathbf{v}_{\mathbf{u},\alpha\beta} \\ \mathbf{v}_{\mathbf{l},\alpha\beta} \end{bmatrix} = -\mathbf{T_M^{-1}} \begin{bmatrix} \mathbf{2v}_{\mathbf{s},\alpha\beta} \\ \mathbf{v}_{\mathbf{c},\alpha\beta} \end{bmatrix}. \tag{7}$$

By replacing the previous expression in Equation (6) and multiplying it by the matrix transformation $\mathrm{T_M}$, it is possible to decouple the output and circulating current models as follows:

$$\begin{bmatrix} \mathbf{L_T} & 0 \\ 0 & \mathbf{L_T} \end{bmatrix} \frac{d}{dt} \begin{bmatrix} \mathbf{i}_{\mathbf{o},\alpha\beta} \\ \mathbf{i}_{\mathbf{c},\alpha\beta} \end{bmatrix} + \begin{bmatrix} \mathbf{R_T} & 0 \\ 0 & \mathbf{R_T} \end{bmatrix} \begin{bmatrix} \mathbf{i}_{\mathbf{o},\alpha\beta} \\ \mathbf{i}_{\mathbf{c},\alpha\beta} \end{bmatrix} = \begin{bmatrix} \mathbf{2v}_{\mathbf{s},\alpha\beta} \\ \mathbf{v}_{\mathbf{c},\alpha\beta} \end{bmatrix} - \begin{bmatrix} \mathbf{2v}_{\mathbf{o},\alpha\beta} \\ \mathbf{0} \end{bmatrix}. \tag{8}$$

The output current is driven by the voltage difference between $\mathrm{v}_{\mathrm{s},\alpha\beta}$ and $\mathrm{v}_{\mathrm{o},\alpha\beta}$, while the circulating current is driven by the drop in voltage in the coupled inductance $\mathrm{v}_{\mathrm{c},\alpha\beta}$.

To simplify the control design, the two decoupled models are represented based on the synchronous reference frame. This is realized by introducing the Park transformation into Equation (8) as follows:

$$\frac{1}{2}\begin{bmatrix} L_T & -\omega_s L_T \\ \omega_s L_T & L_T \end{bmatrix}\frac{d}{dt}\mathbf{i_{o,dq}} + \frac{1}{2}\begin{bmatrix} R_T & 0 \\ 0 & R_T \end{bmatrix}\mathbf{i_{o,dq}} = \mathbf{v_{s,dq}} - \mathbf{v_{o,dq}} \tag{9}$$

$$\begin{bmatrix} L_T & -\omega_s L_T \\ \omega_s L_T & L_T \end{bmatrix}\frac{d}{dt}\mathbf{i_{c,dq}} + \frac{1}{2}\begin{bmatrix} R_T & 0 \\ 0 & R_T \end{bmatrix}\mathbf{i_{c,dq}} = \mathbf{v_{c,dq}}. \tag{10}$$

The decoupled model in matrix notation simplifies the analysis of the converter. Using the *dq* synchronous reference frame, the current components can be easily regulated using proportional integrator (PI) controllers, as seen in Figure 3. Note that the variables R_T and L_T represent single elements and not diagonal matrices, as in Equation (8). Additionally, it is important to mention that a current feedforward is used to eliminate current couplings between the *dq* components.

The references $\mathrm{i}^*_{\mathrm{o,dq}}$ and $\mathrm{i}^*_{\mathrm{c,dq}}$ come from outer control loops, which regulate the average DC voltage level in both arms. The PI controllers process the differences between these references with the current measurements given by the transformation of the current arms in the synchronous reference frame. Finally, the output signals of the controllers are decoupled to obtain the modulated voltages $\mathrm{v}_{\mathrm{u,dq}}$ and $\mathrm{v}_{\mathrm{l,dq}}$.

The relationship between the outer control loops and the current references relies upon the dynamic response of the power flow described in Section 2.2.

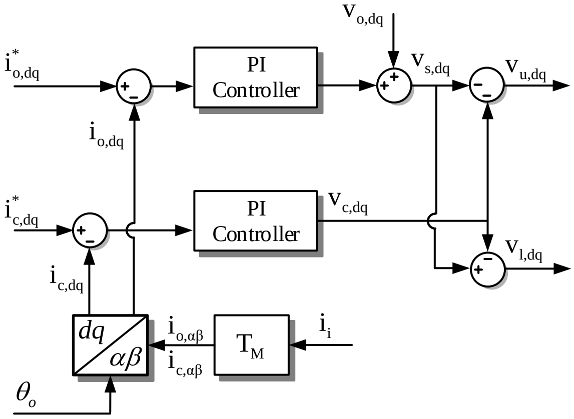

Figure 3. Decoupled current control of the IMMC.

2.2. Instantaneous Power Analysis

There is a direct relationship between the current references and the energy that can be easily inferred from the power analysis. Because the coupling inductance is relatively small, its voltage drop can be neglected. Under this assumption, the instantaneous active power per phase is reduced to:

$$\begin{aligned} p_{u,k} &= v_{u,k} i_{u,k} \\ &= -v_{o,k}\left(\frac{i_{o,k}}{2} + i_{c,k}\right), \end{aligned} \tag{11}$$

$$\begin{aligned} p_{l,k} &= v_{l,k} i_{l,k} \\ &= v_{o,k}\left(-\frac{i_{o,k}}{2} + i_{c,k}\right)' \end{aligned} \tag{12}$$

where $p_{u,k}$ and $p_{l,k}$ are the power generated by the upper and lower arms. Note that the current arms are replaced by the output and circulating currents to provide a clear relationship between the power and the components to be controlled. In order to analyze the three phases, Equations (11) and (12) are turned into the dq reference frame, giving rise to the following expressions.

$$\begin{aligned} p_u &= \frac{3}{2}\left[(v_{ud}+jv_{uq})(i_{ud}-ji_{uq})\right] \\ &= \frac{3}{2}\left[-(v_{od}+jv_{oq})(i_{ud}-ji_{uq})\right] \\ &= \frac{3}{2}\left[-(v_{od}+jv_{oq})\left(\frac{i_{od}-ji_{oq}}{2}+i_{cd}-ji_{cq}\right)\right] \\ &= -\frac{3}{2}\left(\frac{1}{2}v_{od}i_{od}+\frac{1}{2}v_{oq}i_{oq}\right)-\frac{3}{2}(v_{od}i_{cd}+v_{oq}i_{cq}), \end{aligned} \tag{13}$$

$$\begin{aligned} p_l &= \frac{3}{2}\left[\left(v_{ld}+jv_{lq}\right)\left(i_{ld}-ji_{lq}\right)\right] \\ &= \frac{3}{2}\left[(v_{od}+jv_{oq})\left(i_{ld}-ji_{lq}\right)\right] \\ &= \frac{3}{2}\left[(v_{od}+jv_{oq})\left(-\frac{i_{od}-ji_{oq}}{2}+i_{cd}-ji_{cq}\right)\right] \\ &= -\frac{3}{2}\left(\frac{1}{2}v_{od}i_{od}+\frac{1}{2}v_{oq}i_{oq}\right)+\frac{3}{2}(v_{od}i_{cd}+v_{oq}i_{cq}) \end{aligned} \tag{14}$$

The power arms are affected by two components. The first term associates the output voltage with the output current, while the second term associates the output voltage with the circulating current. By adding and subtracting them, it is possible to define the total power delivered to the grid and the power difference under imbalance operations.

$$\begin{aligned} p_T &= p_u + p_l \\ &= -\frac{3}{2}(v_{od}i_{od}+v_{oq}i_{oq}), \end{aligned} \tag{15}$$

$$\begin{aligned} p_\Delta &= p_u - p_l \\ &= -3(v_{od}i_{cd}+v_{oq}i_{cq}), \end{aligned} \tag{16}$$

p_T represents the total power governed by the output current, while p_Δ is the power difference governed by the circulating current. This expression confirms the appearance of a circulating current flowing through the arms when there is a power imbalance.

Using the concept described above, it is possible to define a control architecture for the IMMC that is capable of regulating the output and circulating currents based on two independent systems, where expression (15) provides the output current reference and (16) provides the circulating current.

2.3. General Considerations for Energy Balancing

As described in the previous section, the energy balance is associated with the power flow in the converter. This relationship can also be inferred from the rate of energy change in the DC capacitor of each module. The energy relies upon the difference between the power produced by the external DC sources and the power delivered into the grid. According to [18], the analysis of the energy balance defines the rate of energy change as follows:

$$p_{ci,j} = \frac{C_{sm}}{2}\frac{d}{dt}(v_{dci,j})^2, \tag{17}$$

where C_{sm} is the DC capacitor and $v_{dci,j}$ is the DC voltage in each module. The previous expression denotes that a constant power $p_{ci,j}$ may increase or decrease the voltage in the DC capacitor. Therefore, the power flow between the external DC sources and the power level delivered to the grid must be regulated to avoid high energy changes. External DC sources can be affected by unpredictable changes, as in the case of PV panels, where temperature and irradiation variations modify the power generated. Therefore, the rate of energy change is commanded by the output power $p_{i,j}$.

Considering N modules per arm and a DC voltage level equal to v^{Σ}_{dci}/N, the total rate of energy change is reduced to:

$$\sum_{j=1}^{N} p_{i,j} = \frac{C_{sm}}{2N}\frac{d}{dt}\left(v^{\Sigma}_{dci}\right)^2, \tag{18}$$

where v^{Σ}_{dci} represents the addition of all DC voltages. Using expression (18), the total DC voltage can be regulated through PI controllers, as illustrated in Figure 4. The output of the controllers defines the power p_u and p_l, respectively, which are added and subtracted to obtain the output and difference power. These components are used in Equations (15) and (16) to generate the d components of the current references by multiplying them by K_T and K_Δ.

The outer controllers define the current references based on the addition of all DC voltages per arm. Therefore, energy imbalances between modules are not observed and may trigger possible instabilities when modules generate different power levels. In order to avoid this possible state, a second control loop embedded in each module is required. This second controller adjusts the control signals set by the current controllers, as shown in Figure 3.

To solve this problem, previous works have proposed a control algorithm that regulates the modulated voltage amplitude. According to [18,22], this strategy increases the amplitude level in modules with high power levels and reduces the amplitude in modules with low power levels. However, the capability of withstanding energy imbalances using this approach is limited when the converter works close to overmodulation. The presented control uses a different concept to compensate energy imbalances through a circulating current and a dedicated phase angle in each module.

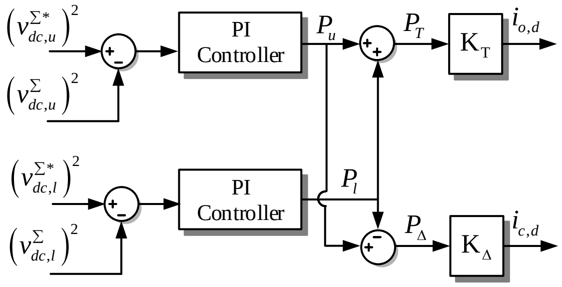

Figure 4. Direct current (DC) voltage control loops for setting the output and circulating current references.

3. Quadrature Voltage Compensation (QVC)

The QVC changes the phase angle of each module to operate under different energy levels. To understand the concept behind the proposed control, it is necessary to go back to the instantaneous power analysis described in Section 2.2. The first term of Equations (13) and (14) regulates the power provided to the grid through the output current, while the second term defines the power imbalance based on the circulating current. This power imbalance can be analyzed in terms of two difference components: the power imbalance between arms and the power imbalance between modules of the same arm. Although they are related, they can be considered as two independent components. The power analysis in [18] demonstrated that the d component of the circulating current comes out when there is a power difference between the arms, while the q component is set to zero. On this occasion, the q component of the circulating current is used in collaboration with a phase angle introduced in the output voltage to compensate energy imbalances between modules, thus increasing the operating range of the converter to withstand higher power levels.

The active power generated by each module can be defined in terms of the modulation index and the DC voltage level, giving rise to the following expressions:

$$\begin{aligned} p_{u,j} = {} & \frac{3}{4}v_{dcu,j}m_{ud,j}\left(\frac{i_{od}}{2}+i_{cd}\right)+ \\ & \frac{3}{4}v_{dcu,j}\left(m_{uq,j}+\Delta m_{uq,j}\right)\left(\frac{i_{oq}}{2}+i_{cq}\right) \\ & = \bar{p}_{u,j}+\Delta p_{u,j} \end{aligned} \tag{19}$$

$$\begin{aligned} p_{l,j} = {} & \frac{3}{4}v_{dcl,j}m_{ld,j}\left(-\frac{i_{od}}{2}+i_{cd}\right)+ \\ & \frac{3}{4}v_{dcl,j}\left(m_{lq,j}+\Delta m_{lq,j}\right)\left(-\frac{i_{oq}}{2}+i_{cq}\right). \\ & = \bar{p}_{l,j}+\Delta p_{l,j} \end{aligned} \tag{20}$$

The average power $\bar{p}_{i,j}$ represents the total power, while the power $\Delta p_{i,j}$ defines the power variation given by the local compensation in each module. This power component is reduced to:

$$\Delta p_{u,j} = \frac{3}{4}v_{dcu,j}\Delta m_{uq,j}\left(\frac{i_{oq}}{2}+i_{cq}\right) \tag{21}$$

$$\Delta p_{l,j} = \frac{3}{4}v_{dcl,j}\Delta m_{lq,j}\left(-\frac{i_{oq}}{2}+i_{cq}\right). \tag{22}$$

The output current i_{oq} controls the reactive power delivered to the grid, while the circulating current i_{cq} controls the power compensation. As the circulating current flows through both arms, it affects all modules. This is why the modulated index $\Delta m_{iq,j}$ provides a tailored power regulation. The presence of a q component in the modulated index creates a phase angle $\gamma_{vi,j}$ defined by:

$$\gamma_{vi,j} = \tan^{-1}\left(\frac{m_{iq,j}+\Delta m_{iq,j}}{m_{id,j}}\right) = \tan^{-1}\left(\frac{v_{iq,j}}{v_{id,j}}\right), \tag{23}$$

where $\gamma_{vi,j}$ is the phase angle of module j in arm i and $v_{idq,j}$ are the dq components of the output voltage. Any variation in $v_{iq,j}$ will change the phase angle $\gamma_{vi,j}$ and, as a consequence, the power compensation. In order to analyze the relationship between the circulating current i_{cq} and the phase angle $\gamma_{vi,j}$, the active power expressions presented in (19) and (20) are analyzed under different values of i_{cq} and $\gamma_{vi,j}$. The results illustrated in Figures 5 and 6 show the cases when both arms operate with balanced and imbalanced power levels.

The phase angle changes from 0 to $\pi/2$, while the circulating current changes from 0 to the nominal current arm. Initially, the phase angle and the circulating current are zero; therefore, there is no power difference between the arms. However, as the phase angle increases, the power in each module decreases. This power change gets higher when the circulating current increases, as illustrated in Figure 5. For instance, a circulating current i_{cq} equal to 0.5 times the nominal current arm requires a phase angle of $\pi/6$ to withstand a power deviation of 40%. Nevertheless, the same power compensation is achieved with a smaller circulating current and a higher phase angle.

In the second analysis, a 40% power difference between the arms produces an inherent circulating current i_{cd}. Figure 6 shows how this power imbalance impacts the initial state when the circulating current i_{cq} and the phase angle $\gamma_{vi,j}$ are zero. The module of the upper arm starts with a power level of 0.5, while the module of the lower arm starts at 0.2.

However, similarly to the previous result, when the circulating current i_{cq} and the phase angle increase, the power provided by each module decreases.

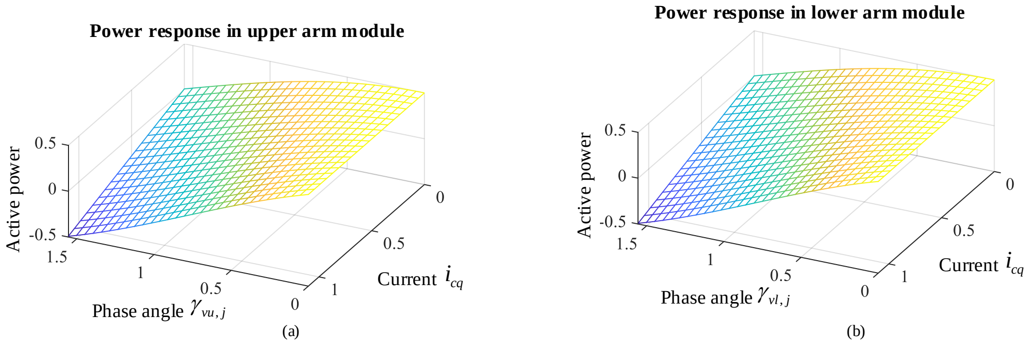

(a) (b)

Figure 5. Active power compensation under circulating current and phase-angle variations with equal power distribution. (**a**) Module in the upper arm, (**b**) module in the lower arm.

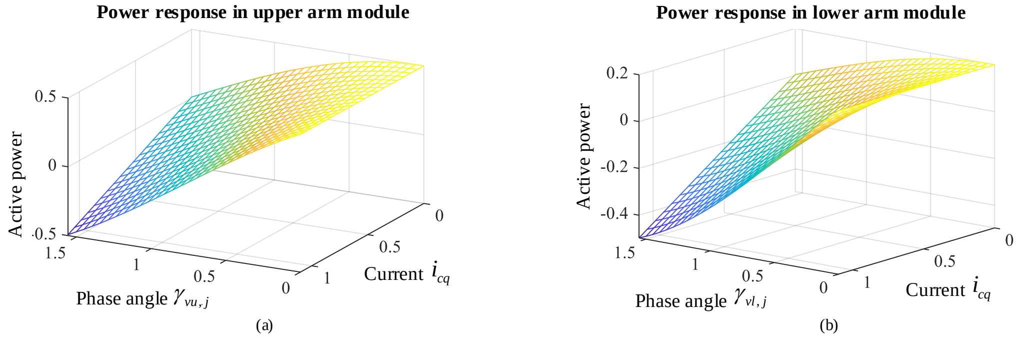

(a) (b)

Figure 6. Active power compensation under circulating current and phase-angle variations with a 40% power difference between both arms. (**a**) Module in the upper arm, (**b**) module in the lower arm.

The concept behind the QVC can be studied using the vector representation shown in Figure 7. The diagram evaluates the interaction of three modules in balanced and imbalanced operation. In balanced operation, all modules generate the same power with output voltages equal to $v_{id,1}$, $v_{id,2}$, and $v_{id,3}$. The combination of these voltages defines the voltage v_o modulated at the AC terminals. Note that the current arm i_i has a phase angle of γ_i degrees.

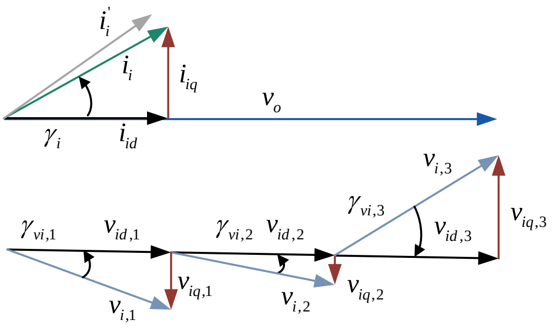

Figure 7. Vector representation of Quadrature Voltage Compensation (QVC).

When there is an energy difference, all modules adjust their output voltages to withstand the power imbalance. After the QVC is used, the output voltages become $v_{i,1}$, $v_{i,2}$, and $v_{i,3}$. These new values are generated by introducing the quadrature voltages $v_{iq,1}$, $v_{iq,2}$, and $v_{iq,3}$, respectively. The quadrature voltages have been selected to maintain the same output voltage v_o as that defined in the balanced operation. Additionally, the current arm i_i has been modified to i_i' through the circulating current i_{cq}. All of these changes modify the angle difference between the current arm and the voltages in the AC terminals of each module, reducing the power generated by modules 1 and 2 and increasing the power in module 3.

The control diagram of the QVC is illustrated in Figure 8. The difference between the DC voltage reference $v^*_{dci,j}$ and the measured voltage is processed through PI controllers. The output of the controller defines the voltage compensation added to the modulated voltage given by the current controllers. Depending on the direction of i_{cq}, the compensation $\Delta m_{i,j}$ is added or subtracted to the quadrature component v_{iq}, thus increasing or reducing the phase angle.

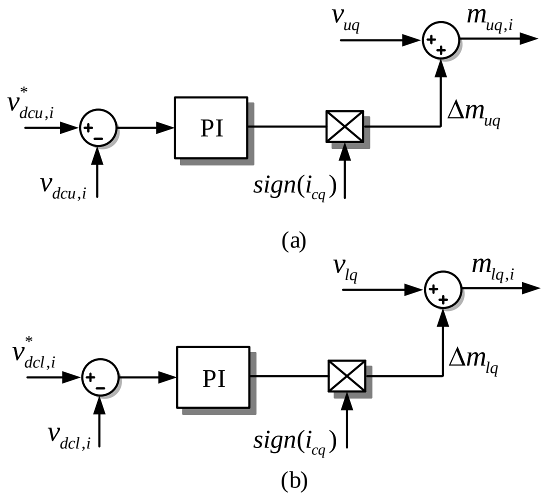

Figure 8. QVC embedded in: (**a**) modules of the upper arm; (**b**) modules of the lower arm.

4. Results

4.1. Simulation Results

The proposed control strategy was validated via simulation results using the three-phase IMMC shown in Figure 1. Each arm has three modules connected to independent PV strings, providing a nominal power of 2 pu. All parameters are described in Table 1.

Table 1. Simulation parameters.

Parameters	Symbol	Simulation
Nominal power	P_o	2 pu
Nominal power per module	$P_{x,i}$	0.33 pu
Grid voltage	v_g	1 pu
Grid frequency	f_g	50 Hz
Number of modules per arm	N	3
DC-link capacitor	C_{sm}	4.7 mF
MPP voltage	v_{mp}	800 V
Transformer inductance	L_T	0.033 pu
Transformer resistance	R_T	0.001 pu
Transformer voltage	v_T	400 V/11 kV
Base parameters		
Base voltage	v_B	33 kV
Base power	P_B	3 MW

Three scenarios are presented to study the steady and dynamic operation of the IMMC. In such cases, the power generated by the PV panels is affected by irradiation changes.

In the first event, the power provided by modules 1 and 2 of the upper arm reduces their power levels by 40%, while module 3 maintains its nominal value. In the second event, module 3 of the lower arm reduces its power by 60%, while the other two modules maintain their nominal power. Finally, module 2 of the lower arm reduces its power by 36%; therefore, all modules of the lower arm operate under different power levels.

Figure 9 shows how the power generated by the converter behaves under such events. At t = 1 s, the power in modules 1 and 2 decreases by 40%, creating a small perturbation in the power provided by module 3. This power change also reduces the power delivered to the grid, as seen in the output power P_o of Figure 9. The power decrease creates an imbalanced operation between modules of the upper arm, demanding a q component of circulating current, which was intentionally set to 33% of the nominal current arm. Figure 10a shows how this event creates a phase shift between the current arms and an increase in the circulating current. It is important to remark that an inherent circulating current i_{cd} appears with a negative value, since the power in the lower arm becomes higher than the power in the upper arm.

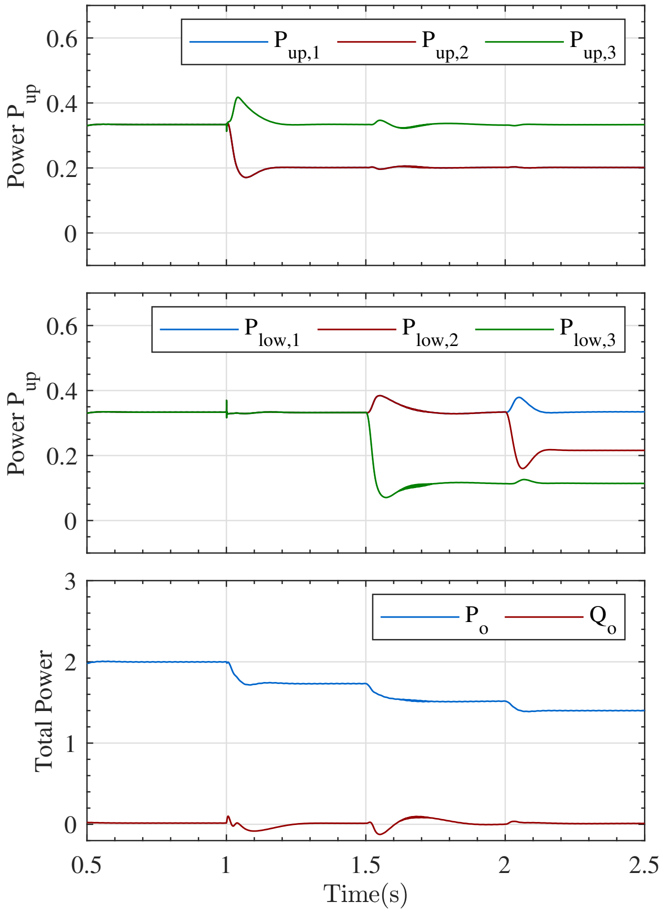

Figure 9. Power response. Active power in upper-arm modules, active power in lower-arm modules, and active and reactive power delivered into the grid.

In the second event, the third module of the lower arm decreases its power by 60%. This large power change reduces the total power delivered to the grid by 17.2%. Although, there is a higher power imbalance; the circulating current provided in the previous event is enough to tolerate such an operation. The power decrease also reduces the current in the lower arm, as shown in Figure 10b, while the current in the upper arm remains at 0.86 pu. Since the power difference between the upper and lower arm is smaller, the circulating current i_{cd} also decreases.

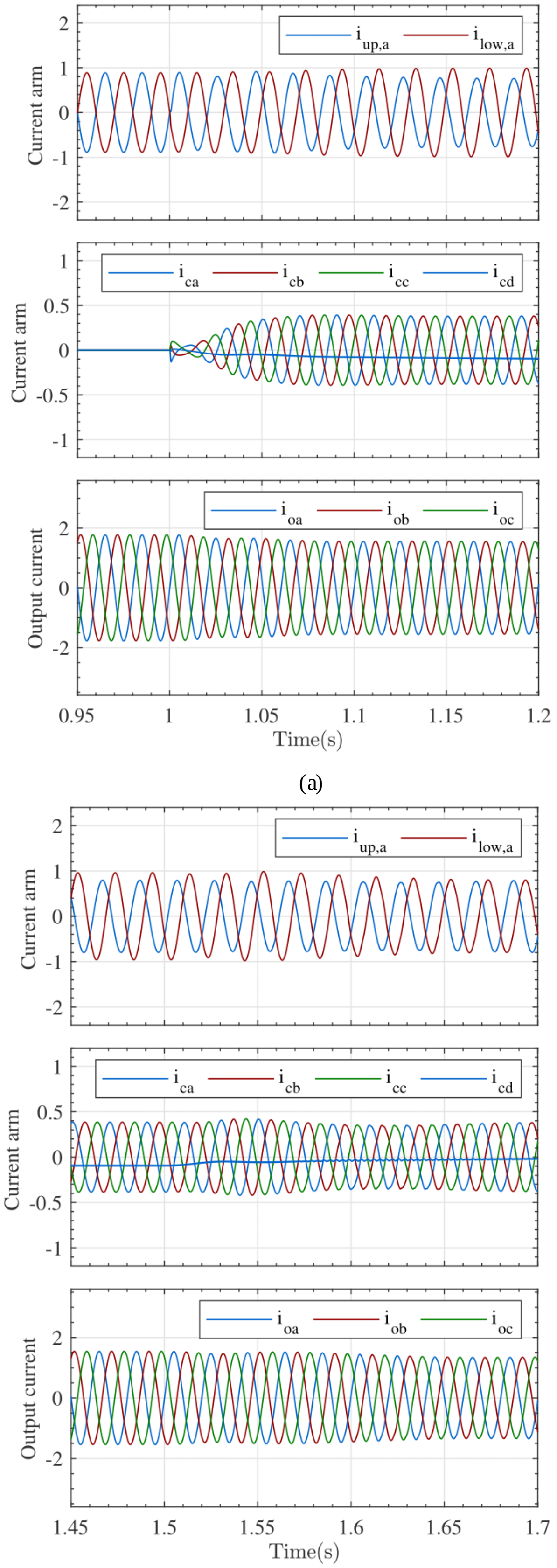

(a)

(b)

Figure 10. Current arms, circulating current, and output current. (**a**) First event, (**b**) second event.

To generate a complete imbalanced operation, at t = 2 s, the third power step is introduced in the second module of the lower arm. This operation is compensated by the proposed control strategy, allowing the converter to generate large power differences between all modules. The performance of the QVC is observed in the modulated voltage illustrated in Figure 11. The first and second modules of the upper arm register the same power imbalance as that of the previous event, so their modulated voltage is shifted with the same phase angle.

On the other hand, the modules of the lower arm register different phase angles after the third event happens. Since module M_{l1} generates the highest power level, it requires the highest modulated voltage amplitude. It is important to mention that a zero-sequence technique based on [23] was used by introducing a third harmonic component, as seen in the modulated voltage waveforms in Figure 11.

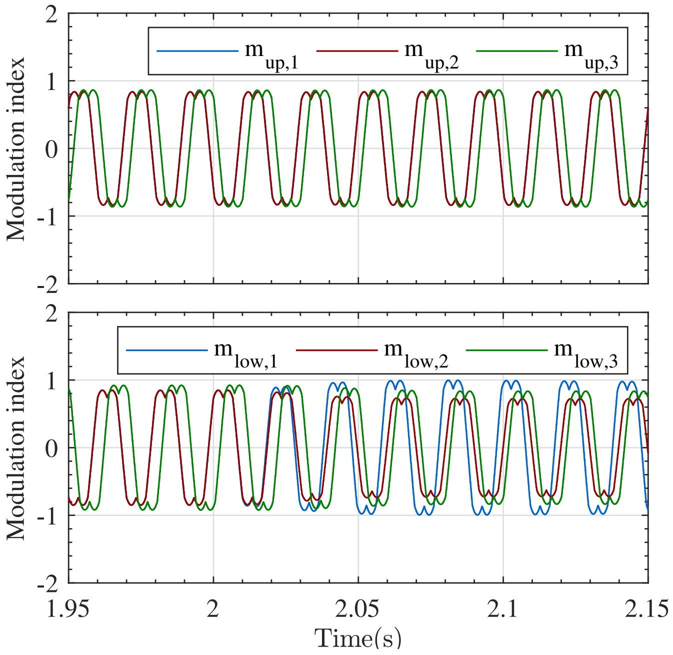

Figure 11. Modulation index in the modules of the upper and lower arms after the third event.

The phase angle set by the local controller depends on the circulating current i_{cq} defined in the general control algorithm. In previous events, the circulating current i_{cq} was set to 33% of the nominal current arm, giving rise to a phase angle of $-29°$ degrees in modules M_{u1} and M_{u2}, while modules M_{l2} and M_{l3} were shifted $36°$ and $-41°$, respectively. In Section 3, it was concluded from the analysis that as the circulating current increases, the phase angle required to compensate a certain power imbalance decreases. This feature reduces the probability of reaching overmodulation.

4.2. Experimental Results

To experimentally validate the operation principle of the proposed control strategy, a downscaled prototype of 4.8 kW of nominal power was used. The configuration illustrated in Figure 12 has two modules per arm, which are connected to low-frequency transformers. Each module is formed by a two-level three-phase inverter with an LC filter in the AC terminals. On the DC side, a programmable DC source (Magna-Power TSD1000-20/36) was connected to series resistors to control the power flow and to emulate four independent PV panels working between the maximum power and the open-circuit operation.

The control algorithms, protection, and switching states were implemented in the control platforms based on the DSPs TMS320F28335 from Texas Instruments. The central platform included the DC voltage and current controllers to set the modulated voltage in the upper and lower arms. Similarly, the DSP controllers embedded in each module integrated protections and the QVC technique to adjust the control signals provided by the central controller according to the local voltage and current states. The communication between the central and local controllers was done through a CAN communication bus. The electrical configuration of the laboratory setup is shown in Figure 12b.

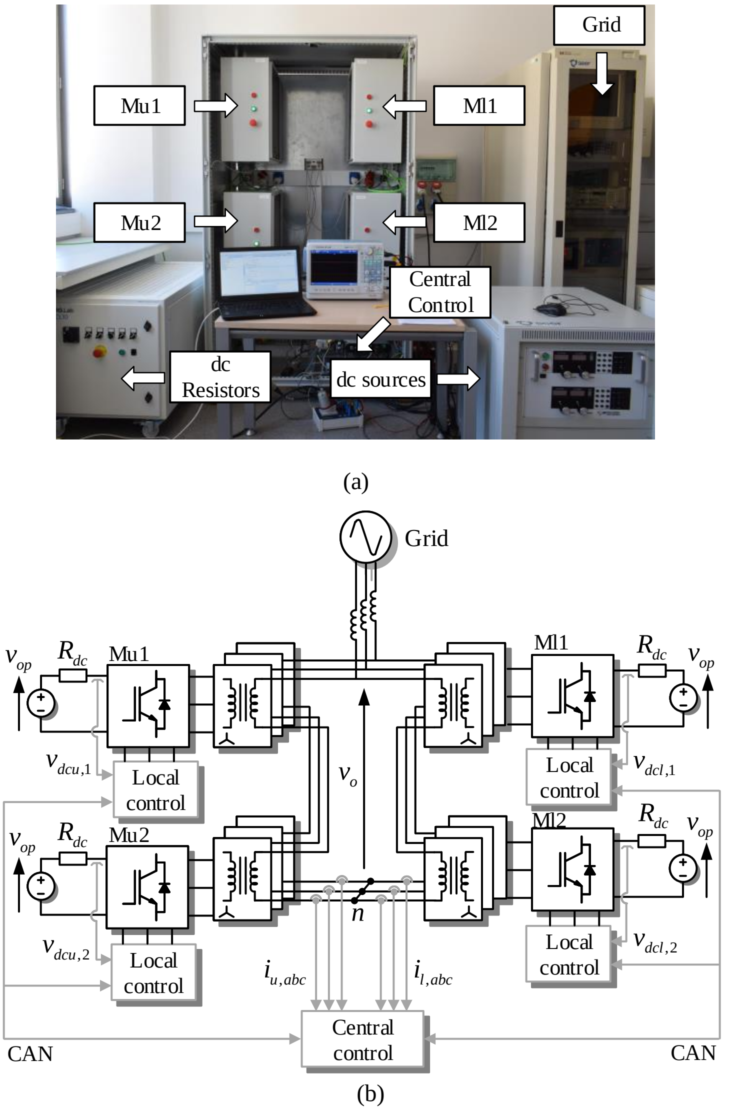

Figure 12. Experimental setup. (**a**) Laboratory prototype, (**b**) electrical circuit diagram.

Two scenarios were studied to validate the operation principles of the QVC technique. In the first case, a DC voltage step was introduced in M_{u1} to create a power imbalance between the modules of the upper arm while the modules of the lower arm generated their nominal power. Then, a second DC voltage step was introduced in module M_{l2} so that both arms had modules at different power levels. The experimental results are shown in Figures 13–16 based on the parameters given in Table 2.

Under nominal conditions, all modules operated at their MPP voltage level, providing 1.2 kW per module. However, after 1.5 s, the DC voltage $v_{dcu,1}$ increased by 40 V, giving rise to a power decrease of 510 W. In order to withstand this power imbalance, a q component of circulating current was set to 35% of the nominal current arm, thus changing the phase angle between both arms, as seen in Figure 14. A focus on the current signals shows how the angle difference between the current arms changed as the circulating current increased. Note that the circulating current was formed by the inherent circulating current i_{cd} given by the power difference between the arms and the current i_{cq} set intentionally to 35% in the central controller.

Table 2. Experimental parameters.

Parameters	Symbol	Simulation
Nominal power	P_o	4.8 kW
Nominal power per module	$P_{x,i}$	1.2 kW
Grid voltage	v_g	320 V
Grid frequency	f_g	50 Hz
Number of modules per arm	N	2
DC-link capacitor	C_{sm}	4.7 mF
DC resistor	$R_{dc,i}$	22.5 Ω
Open circuit voltage	v_{op}	440 V
MPP voltage	v_{mp}	360 V
Inductance LC filter	L_f	3 mH
Capacitance LC filter	C_f	5 μF
Transformer Inductance	L_T	8.3 mH
Transformer voltage	v_T	400 V

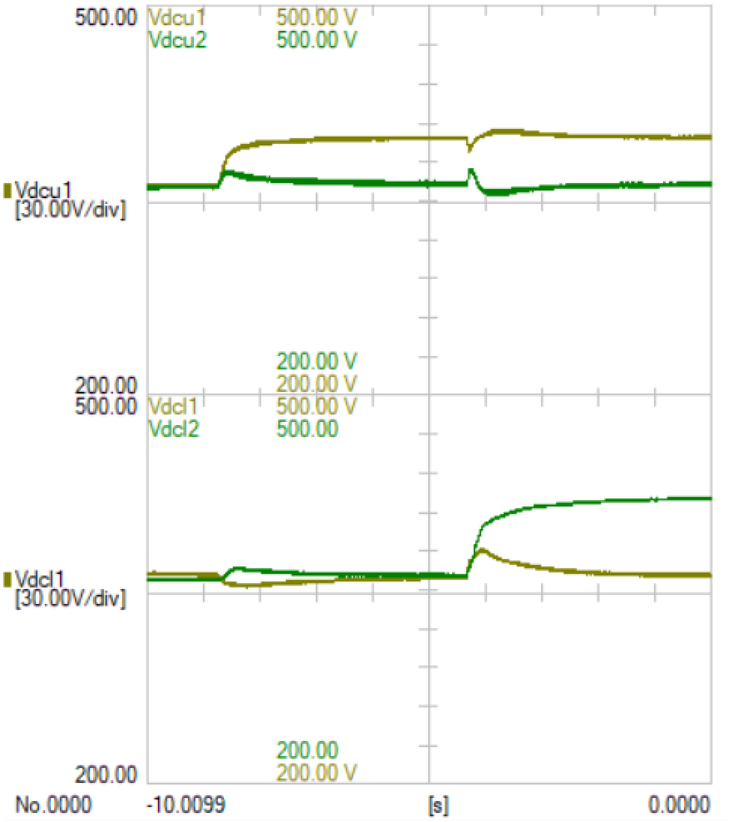

Figure 13. DC voltage step in the first module of the upper arm and the second module of the lower arm.

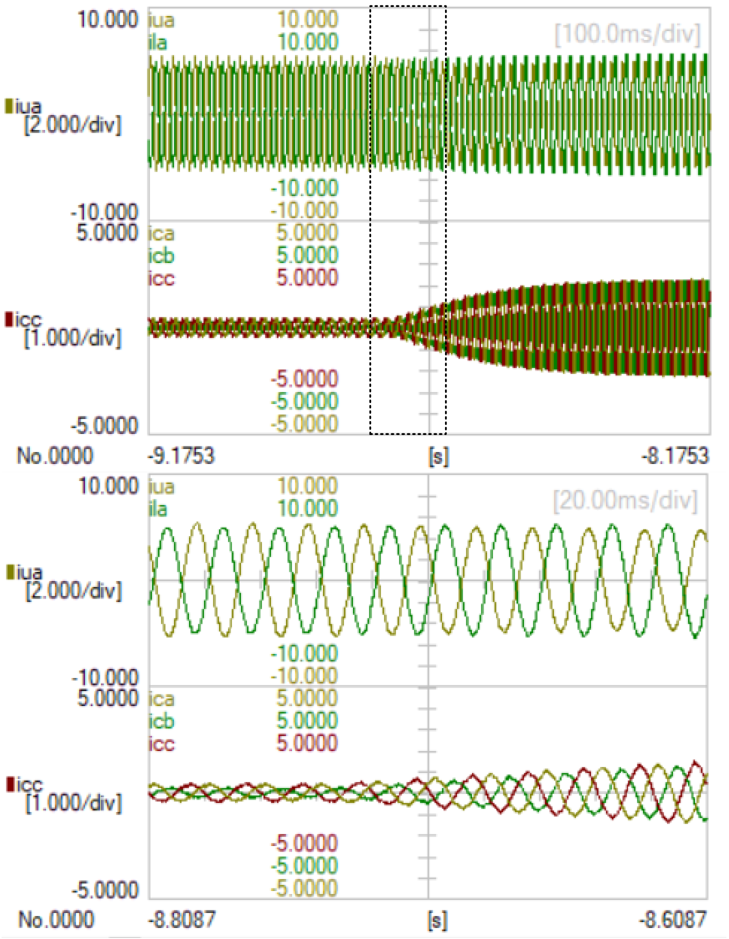

Figure 14. Steady state and dynamic response of current arm and circulating currents in first event.

In the second event, the DC voltage $v_{dcl,2}$ increased by 60 V, reducing the output power P_o by 820 W. This change also reduced the current in the lower arm i_l, as seen in Figure 15. To withstand this second power difference, the circulating current i_{cq} remained as it was in the previous event; therefore, the angle difference between the current arms did not change. There was a small perturbation in the circulating current, while the power provided by module M_{l2} decreased. This behavior was due to the severe change in the d component of the circulating current as a consequence of the power difference between both arms. Even though the circulating current flowed through the converter, it did not have any impact on the output power, as seen in Figure 16, demonstrating that the power delivered to the grid relied upon the output current, while the power imbalance depended on the circulating current.

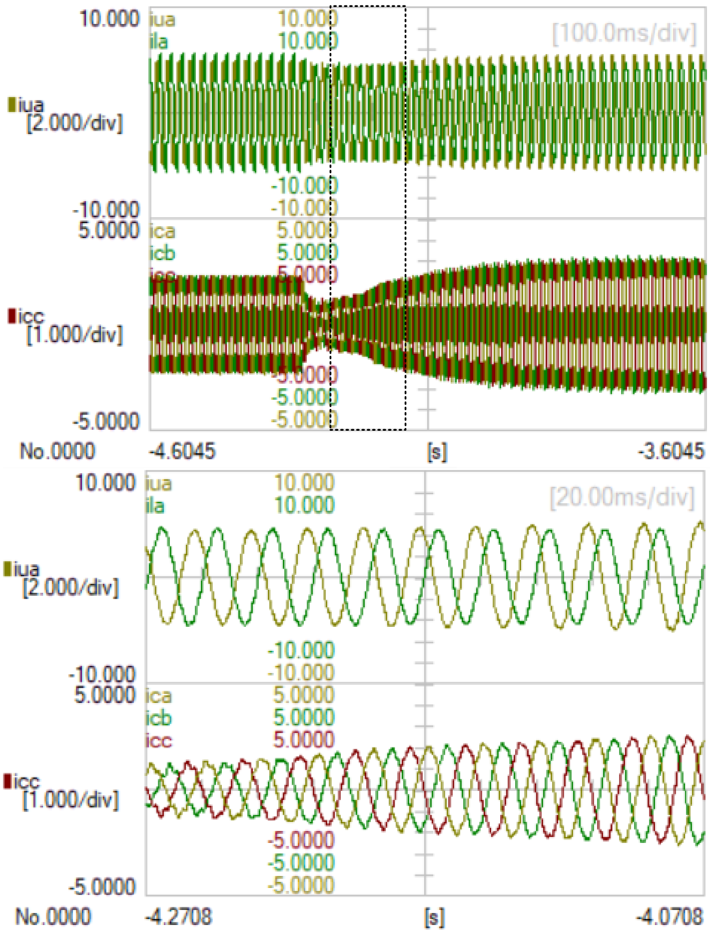

Figure 15. Steady state and dynamic response of current arm and circulating currents in second event.

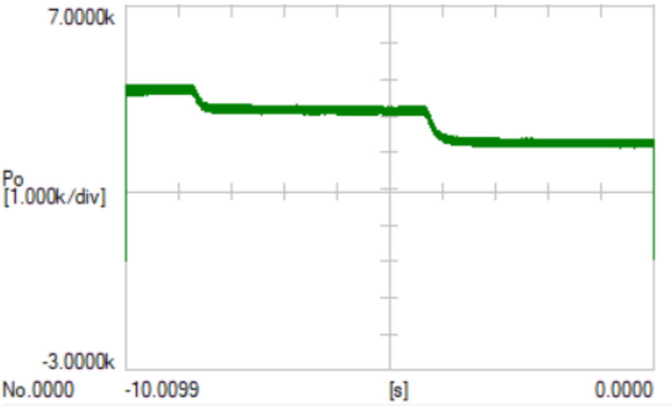

Figure 16. Active power delivered to the grid.

4.3. Comparison between QVC and Amplitude Voltage Compensation (AVC)

In order to demonstrate the capability of the QVC to withstand higher power imbalances compared to the AVC described in [18], a comparative analysis between both control strategies is presented in Figure 17. As in the simulation results, three modules per arm were used. However, on this occasion, an irradiation step was introduced in the first module of the upper arm. The idea is to evaluate the maximum capabilities of withstanding different power imbalances in both control strategies.

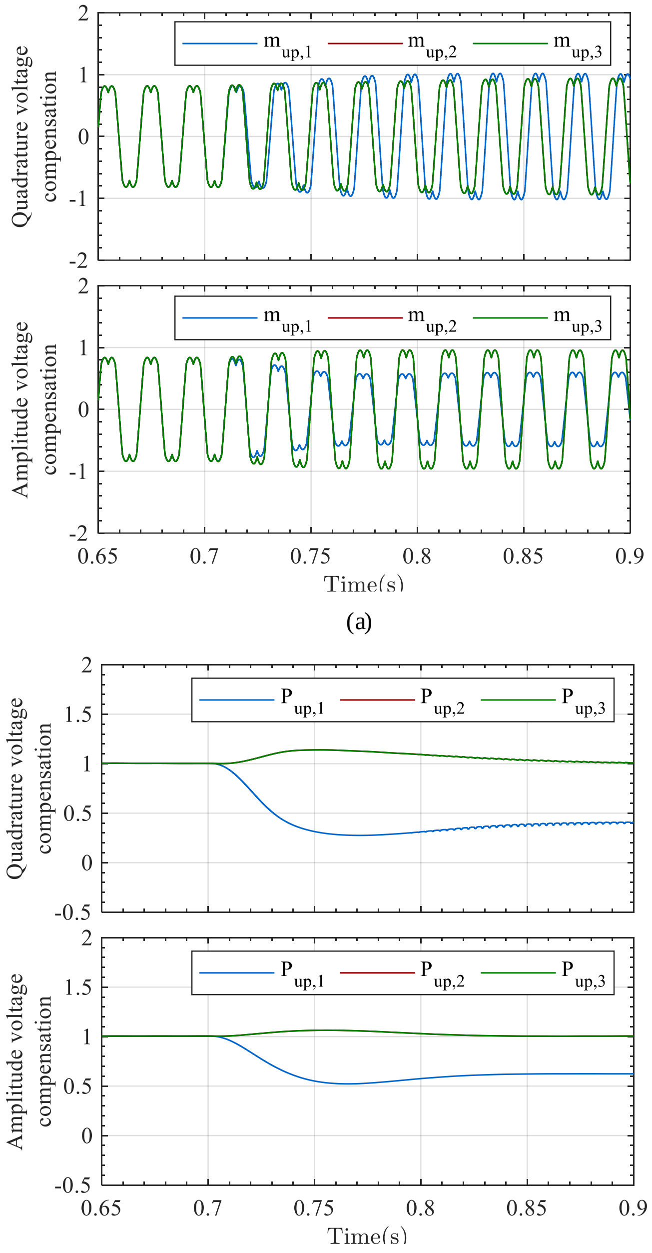

(a)

(b)

Figure 17. Comparative analysis between quadrature and amplitude voltage compensation. (**a**) Modulation index, (**b**) active power per module.

The modulated voltage and the power response of each module are illustrated in Figure 17a,b, respectively. It is clearly observed that the IMMC based on the QVC is able to withstand higher power imbalances compared to the AVC. By using this strategy, the converter tolerates power imbalances of up to 60% before overmodulation with a circulating current i_{cq} = 33% in the nominal current arm, while the AVC is able to withstand a power imbalance of 37%.

5. Conclusions

In this work, the principle of Quadrature Voltage Compensation was proposed for the IMMC, and it was studied and validated with modules operating at different power levels. This control strategy adjusts the modulation index provided by the central control through a circulating current i_{cq} and a phase angle introduced in the output voltages of each module.

In order to evaluate the impact of the QVC, the relationship between the circulating current i_{cq} and the phase angle was analyzed under different values, demonstrating that high levels of circulating current i_{cq} require small phase angles, and vice versa. Simulation and experimental results were presented to evaluate the steady- and dynamic-state operation with modules in balanced and imbalanced power states. Finally, a comparison with AVC was presented to demonstrate the better ability of the QVC to tolerate power imbalances.

Author Contributions: C.V., J.I.C., P.R. contributed equally to this work. All authors have read and agreed to the published version of the manuscript.

Funding: This work was supported by the Ministry of Science Innovation and Universities under the project RTI-2018-100921-B-21 and by the European Commission under the projects FLEXITRANSTORE H2020-LCE-2016-2017-SGS-774407 and INTERRFACE H2020-LC-SC3-2018-ES-SCC-824330.

Conflicts of Interest: The authors declare no conflict of interest.

Abbreviations

The following abbreviations are used in this manuscript:

PV	Photovoltaic
CTMI	Cascaded-transformer multilevel inverter
DC	Direct current
AC	Alternating current
IMMC	Isolated multi-modular converter
AVC	Amplitude voltage compensation
QVC	Quadrature voltage compensation
PI	Proportional integrator

Nomenclature

The following nomenclature is used in the figures and tables of this manuscript:

L_T	Coupling inductance
R_T	Transformer losses
$i_{u,k}$	Current in upper arm of phase *k*
$i_{l,k}$	Current in lower arm of phase *k*
$i_{o,k}$	Output current in phase *k*
$i_{c,k}$	Circulating current in phase *k*
$v_{o,k}$	Output voltage in phase *k*
$v_{u,k,j}$	Voltage in power module *j* of upper arm
$v_{l,k,j}$	Voltage in power module *j* of lower arm
v_c	Drop in voltage in coupling inductance
v_s	Voltage difference between upper and lower arms
L_s	Grid inductance
R_s	Grid resistance
$v_{g,k}$	Grid voltage in phase *k*
n	Neutral point in IMMC
$v_{dci,j}$	DC voltage in module *j* of arm *i*
$\mathrm{T_c}$	Clark transformation
$\mathrm{T_M}$	Decoupling matrix transformation
$\mathrm{R_T}$, $\mathrm{L_T}$	Diagonal matrices of transformer losses and coupling inductance
$\mathbf{i}_{\mathbf{x},\alpha\beta}$, $\mathbf{v}_{\mathbf{x},\alpha\beta}$	Vector notation of current and voltage signals in $\alpha\beta$ reference frame
$\mathbf{i}_{\mathbf{x},\mathbf{dq}}$, $\mathbf{v}_{\mathbf{x},\mathbf{dq}}$	Vector notation of current and voltage signals in dq reference frame
x	Subindex of arm and output signals
$p_{u,k}$, $p_{l,k}$	Instantaneous power in upper and lower arm of phase *k*
p_u, p_l	Three-phase instantaneous power
p_T	Total power
p_Δ	Power difference
$p_{ci,j}$	Instantaneous power in DC capacitor

C_{sm}	DC capacitor
v_{dci}^{Σ}	Total DC voltage in arm i
$\mathrm{K_T}$	Constant to convert instantaneous power p_T into output current
K_{Δ}	Constant to convert instantaneous power p_{Δ} into circulating current
$m_{u,dq}, m_{l,dq}$	Modulation index in dq reference frame
Δm_{uq}, Δm_{lq}	Deviation of modulation index in upper and lower arms
$\Delta p_{i,j}$	Deviation of instantaneous power in module j
$\bar{p}_{i,j}$	Average power in module j
N	Number of power modules per arm
$\gamma_{vi,j}$	Phase angle of module j in arm i
f_g	Grid frequency
v_{mp}	DC voltage at maximum power
v_T	Transformer voltage
v_B	Base voltage
p_B	Base power
L_f	Inductance LC filter
C_f	Capacitance LC filter

References

1. Carrasco, J.M.; Franquelo, L.G.; Bialasiewicz, J.T.; Galván, E.; PortilloGuisado, R.C.; Prats, M.M.; León, J.I.; Moreno-Alfonso, N. Power-Electronic Systems for the Grid Integration of Renewable Energy Sources: A Survey. *IEEE Trans. Ind. Electron.* **2006**, *53*, 1002–1016.
2. Leon, J.I.; Vazquez, S.; Kouro, S.; Franquelo, L.G.; Carrasco, J.M.; Rodriguez, J. Unidimensional Modulation Technique for Cascaded Multilevel Converters. *IEEE Trans. Ind. Electron.* **2009**, *56*, 2981–2986. [CrossRef]
3. Babaei, E. A Cascade Multilevel Converter Topology With Reduced Number of Switches. *IEEE Trans. Power Electron.* **2008**, *23*, 2657–2664. [CrossRef]
4. Wang, K.; Zhu, R.; Wei, C.; Liu, F.; Wu, X.; Liserre, M. Cascaded Multilevel Converter Topology for Large-Scale Photovoltaic System With Balanced Operation. *IEEE Trans. Ind. Electron.* **2019**, *66*, 7694–7705. [CrossRef]
5. Zhao, W.; Choi, H.; Konstantinou, G.; Ciobotaru, M.; Agelidis, V.G. Cascaded H-bridge multilevel converter for large-scale PV grid-integration with isolated DC-DC stage. In Proceedings of the 2012 3rd IEEE International Symposium on Power Electronics for Distributed Generation Systems (PEDG), Aalborg, Denmark, 25–28 June 2012; pp. 849–856.
6. Busquets-Monge, S.; Rocabert, J.; Rodriguez, P.; Alepuz, S.; Bordonau, J. Multilevel Diode-Clamped Converter for Photovoltaic Generators With Independent Voltage Control of Each Solar Array. *IEEE Trans. Ind. Electron.* **2008**, *55*, 2713–2723. [CrossRef]
7. Essakiappan, S.; Krishnamoorthy, H.S.; Enjeti, P.; Balog, R.S.; Ahmed, S. Multilevel Medium-Frequency Link Inverter for Utility Scale Photovoltaic Integration. *IEEE Trans. Power Electron.* **2015**, *30*, 3674–3684. [CrossRef]
8. Achanta, P.K.; Johnson, B.B.; Seo, G.; Maksimovic, D. A Multilevel DC to Three-Phase AC Architecture for Photovoltaic Power Plants. *IEEE Trans. Energy Convers.* **2019**, *34*, 181–190 . [CrossRef]
9. Acharya, A.B.; Ricco, M.; Sera, D.; Teoderscu, R.; Norum, L.E. Performance Analysis of Medium-Voltage Grid Integration of PV Plant Using Modular Multilevel Converter. *IEEE Trans. Energy Convers.* **2019**, *34*, 1731–1740. [CrossRef]
10. Panda, A.K.; Suresh, Y. Performance of cascaded multilevel inverter by employing single and three-phase transformers. *IET Power Electron.* **2012**, *5*, 1694–1705. [CrossRef]
11. Gandomi, A.A.; Saeidabadi, S.; Hosseini, S.H.; Babaei, E.; Gandomi, Y.A. Flexible transformer-based multilevel inverter topologies. *IET Power Electron.* **2019**, *12*, 578–587. [CrossRef]
12. Behara, S.; Sandeep, N.; Yaragatti, U.R. Design and Implementation of Transformer-Based Multilevel Inverter Topology With Reduced Components. *IEEE Trans. Ind. Appl.* **2018**, *54*, 4632–4639. [CrossRef]
13. Khoun jahan, H.; Zare, K.; Abapour, M. Verification of a Low Component Nine-Level Cascaded-Transformer Multilevel Inverter in Grid-Tied Mode. *IEEE J. Emerg. Sel. Top. Power Electron.* **2018**, *6*, 429–440. [CrossRef]
14. Lopez-Santos, O.; Jacanamejoy-Jamioy, C.A.; Salazar-D'Antonio, D.F.; Corredor-Ramírez, J.R.; Garcia, G.; Martinez-Salamero, L. A Single-Phase Transformer-Based Cascaded Asymmetric Multilevel Inverter with Balanced Power Distribution. *IEEE Access* **2019**, *7*, 98182–98196. [CrossRef]
15. Lee, J.; Sim, H.; Kim, J.; Lee, K. Combination Analysis and Switching Method of a Cascaded H-Bridge Multilevel Inverter Based on Transformers With the Different Turns Ratio for Increasing the Voltage Level. *IEEE Trans. Ind. Electron.* **2018**, *65*, 4454–4465. [CrossRef]
16. Kang, F.-S. Modified multilevel inverter employing half- and full-bridge cells with cascade transformer and its extension to photovoltaic power generation. *Electr. Power Syst. Res.* **2010**, *80*, 1437–1445. [CrossRef]
17. Da Costa Bahia, F.A.; Jacobina, C.B.; Rocha, N.; De Sousa, R.P.R. Cascaded Transformer Multilevel Inverters with Asymmetrical Turns Ratios Based on NPC. *IEEE Trans. Ind. Electron.* **2019**, *67*, 6387–6397.
18. Verdugo, C.; Candela, J.I.; Blaabjerg, F.; Rodriguez, P. Three-Phase Isolated Multimodular Converter in Renewable Energy Distribution Systems. *IEEE J. Emerg. Sel. Top. Power Electron.* **2020**, *8*, 854–865. [CrossRef]

19. Yu, Y.; Konstantinou, G.; Hredzak, B.; Agelidis, V.G. Power Balance of Cascaded H-Bridge Multilevel Converters for Large-Scale Photovoltaic Integration. *IEEE Trans. Power Electron.* **2016**, *31*, 292–303. [CrossRef]
20. Barrena, A.; Marroyo, L.; Rodriguez Vidal, M.Á.; Torrealday Apraiz, J.R. Individual Voltage Balancing Strategy for PWM Cascaded H-Bridge Converter-Based STATCOM. *IEEE Trans. Ind. Electron.* **2008**, *55*, 21–29. [CrossRef]
21. Liu, Z.; Liu, B.; Duan, S.; Kang, Y. A Novel DC Capacitor Voltage Balance Control Method for Cascade Multilevel STATCOM. *IEEE Trans. Power Electron.* **2012**, *27*, 14–27. [CrossRef]
22. Verdugo, C.; Kouro, S.; Rojas, C.A.; Perez, M.A.; Meynard, T.; Malinowski, M. Five-Level T-type Cascade Converter for Rooftop Grid-Connected Photovoltaic Systems. *Energies* **2019**, *12*, 1743. [CrossRef]
23. Rivera, S.; Kouro, S.; Wu, B.; Leon, J.I.; Rodríguez, J.; Franquelo, L.G. Cascaded H-bridge multilevel converter multistring topology for large scale photovoltaic systems. In Proceedings of the 2011 IEEE International Symposium on Industrial Electronics, Gdansk, Poland, 27–30 June 2011; pp. 1837–1844.